ADVANCED ELECTRONIC MATERIALS
www.advelectronicmat.de

# Manipulation of Ni Interstitials for Realizing Large Power Factor in TiNiSn-Based Materials

*Wuyang Ren, Hangtian Zhu, Jun Mao, Li You, Shaowei Song, Tian Tong, Jiming Bao, Jun Luo, Zhiming Wang,* and Zhifeng Ren**

**Defect engineering has been identified as an effective strategy for improving thermoelectric performance by tailoring electron and phonon transport. TiNiSn is unique due to its naturally formed Ni interstitials, where the interstitial atoms enable strong phonon scattering that results in reduced lattice thermal conductivity, although an adverse effect on mobility is inevitable. Rather than pursuing the conventional strategy of strengthening the interstitial scattering to improve the performance of TiNiSn-based materials, an attempt is made to minimize the atomic disorder in order to enhance the mobility, which in turn favors a higher power factor. The altered bandgap, and electrical and thermal properties demonstrate that the interstitials can be effectively controlled by intentionally reducing the amount of Ni. Benefiting from the manipulation of the interstitials, significantly enhanced mobility is achieved in the Ni-deficient composition, resulting in peak power factor of ≈50 μW cm$^{-1}$ K$^{-2}$, which is comparable to the best n-type half-Heusler compounds. Additionally, the well-designed composition employing Ni interstitial manipulation and heavy-element doping exhibits peak *ZT* of ≈0.73, higher than that of all other reported TiNiSn-based materials. The unique role of interstitials in either electron or phonon transport is emphasized, and further encouragement for engineering thermoelectric properties by manipulating intrinsic disorder, especially in materials with complex structures, is provided.**

## 1. Introduction

Half-Heusler compounds have been discovered with various beneficial characteristics[1–3] (e.g., high power factor, novel orbital interactions, unique atomic arrangement, robust mechanical properties, and low toxicity) for use as efficient thermoelectric materials working at high temperatures (800–1000 K).[4–9] The most fascinating property is their high power factor originating from the weak electron-acoustic phonon couplings induced by the symmetry-protected orbital interactions, which favors a delicate relationship between high conductivity and a large Seebeck coefficient.[3] Correspondingly, a record-high power factor (with the peak value ≈100 μW cm$^{-1}$ K$^{-2}$ obtained in Ti-doped NbFeSb-based materials) highlights the superior electrical performance of the half-Heusler materials.[10] Among this class of materials, TiNiSn-based compounds have generated much interest,[11–14] although their relatively low carrier mobility (below 20 cm$^2$ V$^{-1}$ s$^{-1}$) and inferior power factor (≈30 μW cm$^{-1}$ K$^{-2}$) have impeded their development for high-performance.[15–20] Since their counterpart MNiSn (M = Zr, Hf) compounds commonly possess large power factor values (≈50 μW cm$^{-1}$ K$^{-2}$) resulting from higher carrier mobility (over 30 cm$^2$ V$^{-1}$ s$^{-1}$),[21–23] it is reasonable that the power factor of TiNiSn-based compounds can be improved via carrier mobility enhancement.

TiNiSn has a MgAgAs-type structure[24] comprised of four interpenetrating facecentered cubic (fcc) sublattices, as shown in **Figure 1**a, where Ti, Ni, and Sn are located at the Wyckoff positions: Ti at 4a (0, 0, 0), Ni at 4c (1/4, 1/4, 1/4), and Sn at 4b (1/2, 1/2, 1/2), leaving the fourth fcc sublattice at 4d (3/4, 3/4, 3/4) unoccupied. When this vacant position is filled with extra Ni, the full-Heusler structure $TiNi_2Sn$ is formed, as shown in Figure 1b. In this half-Heusler material, Ni plays a unique role in either phonon or electron transport. Based on first-principle calculations, interstitial Ni atoms are energetically more favorable than other types of defects.[19,25] Neutron diffraction results have also confirmed partial occupancy of the 4d position by a small amount of Ni in the 1:1:1 stoichiometric TiNiSn.[15,20]

W. Y. Ren, Prof. Z. M. Wang
Institute of Fundamental and Frontier Sciences
University of Electronic Science and Technology of China
Chengdu 610054, China
E-mail: zhmwang@gmail.com

W. Y. Ren, Dr. H. T. Zhu, Dr. J. Mao, L. You, S. W. Song, Prof. Z. F. Ren
Department of Physics and Texas Center for Superconductivity
University of Houston
Houston, TX 77204, USA
E-mail: zren@uh.edu

L. You, Prof. J. Luo
School of Materials Science and Engineering
Shanghai University
Shanghai 200444, China

T. Tong, Prof. J. M. Bao
Department of Electrical and Computer Engineering
University of Houston
Houston, TX 77204, USA

The ORCID identification number(s) for the author(s) of this article can be found under https://doi.org/10.1002/aelm.201900166.

**DOI: 10.1002/aelm.201900166**

 

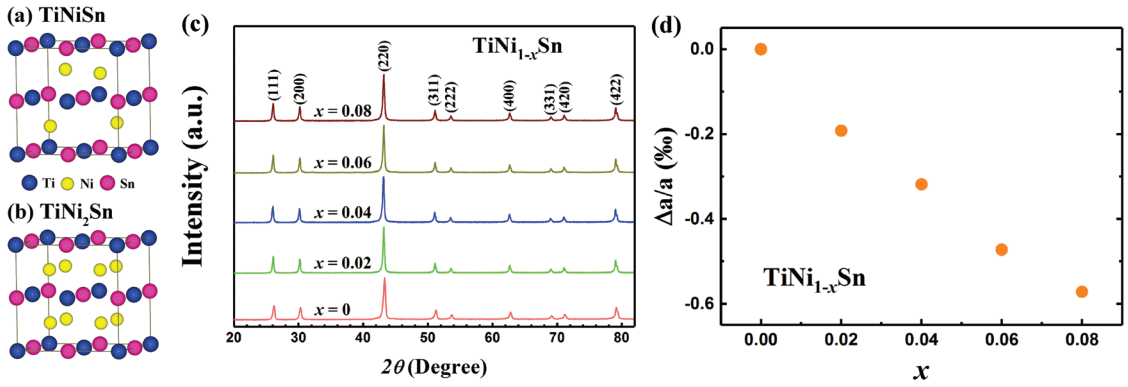


**Figure 1.** Crystal structure of a) half-Heusler TiNiSn and b) full-Heusler $TiNi_2Sn$. c) XRD results and d) variation in lattice parameter $\Delta a/a$ for $TiNi_{1-x}Sn$ ($x$ = 0, 0.02, 0.04, 0.06, and 0.08).

Generally, lattice thermal conductivity can be greatly suppressed by introducing interstitial atoms,[26–29] e.g., interstitial zinc in $Zn_4Sb_3$[30] and multiple fillers in skutterudites.[31] As a consequence, the room-temperature lattice thermal conductivity of undoped TiNiSn is only around 5–6 W $K^{-1}$ $m^{-1}$,[15,16] quite different from other undoped half-Heusler materials (e.g., NbFeSb[7] and ZrCoSb[8]) with room-temperature lattice thermal conductivity values over 10 W $K^{-1}$ $m^{-1}$. Besides the reduction of thermal conductivity, the impact of Ni interstitials on electron transport is also considerable, where the interstitial atoms act as electron donors, making undoped TiNiSn exhibit n-type behavior.[20,32] Moreover, Tang et al. clarified the limited solubility of excess Ni in TiNiSn by experimentally investigating the Ti–Ni–Sn phase diagram in detail.[16] Therefore, previous studies have mainly focused on increasing the amount of interstitial Ni atoms to simultaneously suppress lattice thermal conductivity and tune electron concentration before the decomposition into a two-phase mixture of half-Heusler and full-Heusler compounds. However, such disorder induced by Ni interstitials adversely affects the electron mobility, which could be the origin of the inferior power factor of TiNiSn-based materials.

In contrast to the conventional strategy of strengthening interstitial defect scattering, here we report our effort to minimize this atomic disorder in order to obtain higher electron mobility, which in turn leads to power factor improvement. The manipulation of the Ni interstitials was achieved by artificially decreasing the Ni content based on the evidence from distinct differences of structural, electrical, and thermal properties between TiNiSn (Ni-sufficient composition) and $TiNi_{0.92}Sn$ (Ni-deficient composition). Considering the increased lattice thermal conductivity in the Ni-deficient composition, the partial substitution of tantalum for titanium was employed as an alternative approach to lower lattice thermal conductivity, which is also capable of optimizing carrier concentration. Benefiting from the manipulation of the Ni interstitials, the Hall mobility in the Ni-deficient samples can be enhanced to ≈30 $cm^2$ $V^{-1}$ $s^{-1}$, contributing to a significantly improved power factor over the whole temperature range, e.g., the room-temperature and peak values show improvement of ≈47% and 35%, respectively, compared to the Ni-sufficient composition with a similar carrier concentration. Moreover, our well-designed TiNiSn-based material, employing both Ni interstitial manipulation and Ta doping for Ti, exhibits a peak $ZT$ of ≈0.73, exceeding that reported for any other TiNiSn-based thermoelectric materials.

## 2. Results and Discussion

As mentioned above, the Ni content was artificially reduced to manipulate the Ni interstitial defects, resulting in the compositions $TiNi_{1-x}Sn$ ($x$ = 0, 0.02, 0.04, 0.06, and 0.08). The pure half-Heusler phase of $TiNi_{1-x}Sn$ can be observed from X-ray diffraction (XRD) results, as shown in Figure 1c. Previous calculation[19] and experimental[20] results demonstrated an expansion of the lattice parameter as a result of the presence of Ni interstitials. As clearly shown in Figure 1d, $TiNi_{0.92}Sn$ exhibits a shrinkage of the lattice parameter in comparison to TiNiSn. Regardless of the Ni-sufficient or -deficient composition, each element is evenly distributed according to energy-dispersive X-ray spectroscopy (EDS) mapping (Figure S2, Supporting Information).

The temperature-dependent electrical and thermal properties of $TiNi_{1-x}Sn$ are shown in **Figure 2**. Typically, the Seebeck coefficient ($S$) of undoped half-Heusler compounds (e.g., NbFeSb,[7] ZrCoSb,[8] and ZrCoBi[9]) is quite low at room temperature since the two types of carriers contribute, resulting in the Fermi level being close to the middle of the bandgap. The natural self-doping by Ni interstitials raises the Fermi level toward the conduction-band minimum,[32] and hence the nominal composition TiNiSn shows n-type behavior with $|S|$ of ≈150 μV $K^{-1}$ at room temperature. As clearly shown in Figure 2a, the $|S|$ at room temperature falls with $x$. This phenomenon does not rely on the increased electron concentration because the amount of electron donors, namely Ni interstitials, is reduced. Furthermore, detailed theoretical calculations have pointed out that other kinds of defects are either energetically unfavorable or charge neutral.[19,32] In this scenario, a minority carrier should be taken into account. The actual Seebeck coefficient ($\alpha$) is the net effect of the two types of carriers, given by

$$\alpha = \frac{S_n\sigma_n + S_p\sigma_p}{\sigma_n + \sigma_p} \quad (1)$$

where $S_n$ ($S_p$) and $\sigma_n$ ($\sigma_p$) are the partial Seebeck coefficient and electrical conductivity for electrons (holes), respectively.[33]

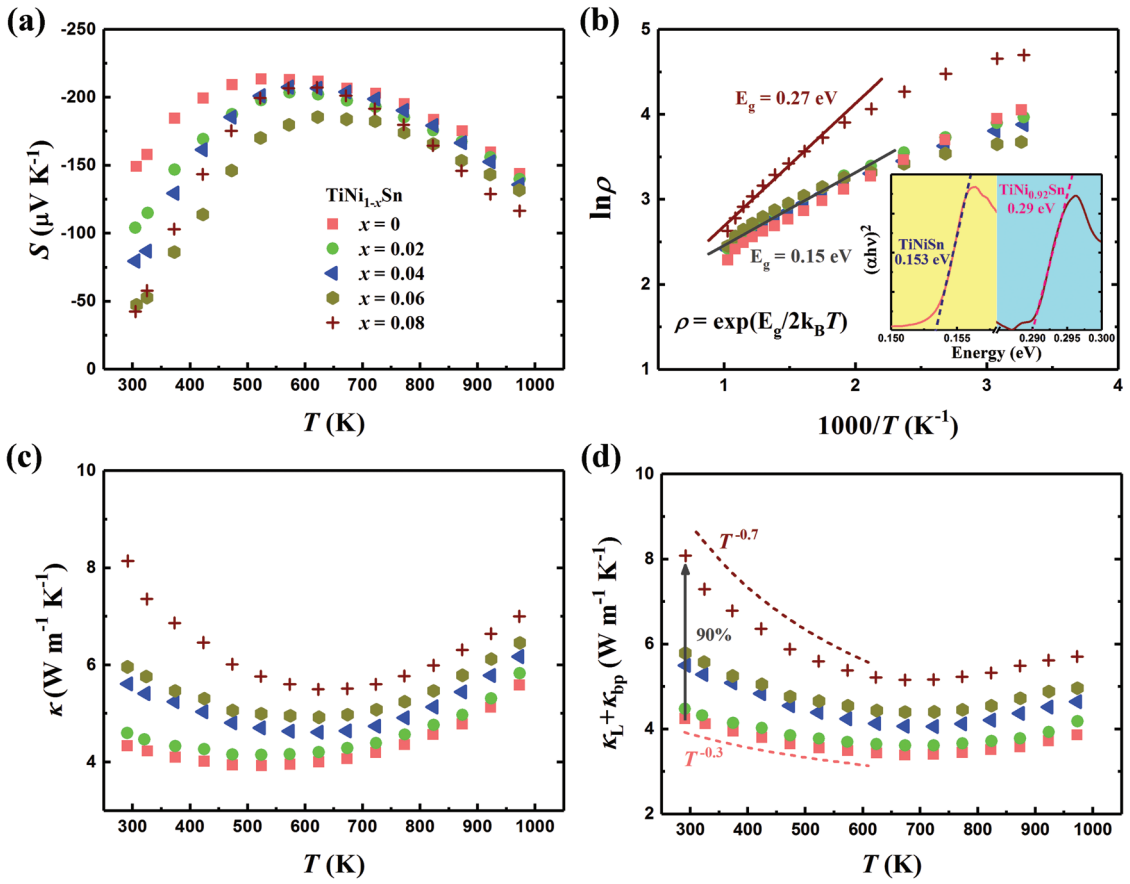


**Figure 2.** Temperature-dependent electrical and thermal properties of $TiNi_{1-x}Sn$. a) Seebeck coefficient, b) electrical resistivity (in units of μΩ m), c) thermal conductivity, and d) the sum of lattice and bipolar thermal conductivity. The inset of (b) shows the optical bandgap for TiNiSn and $TiNi_{0.92}Sn$ at room temperature.

For $TiNi_{0.92}Sn$, there are fewer Ni interstitials to supply electrons, so the opposite contribution of the minority carrier to the actual Seebeck coefficient cannot be neglected. As a result, the Fermi level in $TiNi_{0.92}Sn$ is pushed to the mid bandgap, leading to only weak n-type behavior in $TiNi_{0.92}Sn$. Correspondingly, the higher resistivity ($\rho$) of $TiNi_{0.92}Sn$ than that of other compositions is reasonable. Furthermore, the bandgap ($E_g$) can be extracted from the temperature dependence of the resistivity according to $\rho = \exp(E_g/2k_BT)$ ($500 < T < 1000$ K).[34] The extracted bandgap of $TiNi_{0.92}Sn$ increases to ≈0.27 eV and is ≈0.15 eV for other compositions, as shown in Figure 2b. It should be noted that the simple Goldsmid–Sharp formula is inadequate for revealing the true bandgap of this system due to the large difference in the weighted mobility between electrons and holes.[35] Based on the optical measurements shown in the inset of Figure 2b, the observed bandgap values of TiNiSn and $TiNi_{0.92}Sn$ are ≈0.15 and ≈0.29 eV, respectively, further confirming the variation of the bandgap. In addition, the reported value for TiNiSn in a range of 0.12–0.15 eV[34,36] is consistent with our result. The shrinkage of the bandgap can be mostly ascribed to the Ni interstitials–induced "in-gap electronic states," which is supported by the X-ray photoelectron spectroscopy analysis and density functional theory calculations.[19,32,37]

The temperature-dependent total thermal conductivity ($\kappa$) of $TiNi_{1-x}Sn$ is plotted in Figure 2c, which includes the electronic, lattice, and bipolar contributions. The electronic thermal conductivity ($\kappa_e$) can be calculated according to the Wiedemann–Franz relation, $\kappa_e = L\sigma T$, where $L$ and $\sigma$ are the Lorenz number and electrical conductivity, respectively. By subtracting $\kappa_e$ from $\kappa$, the sum of lattice and bipolar thermal conductivity ($\kappa_L + \kappa_{bp}$) is presented in Figure 2d, which shows that the lattice thermal conductivity of $TiNi_{0.92}Sn$ is 90% higher than that of TiNiSn at room temperature. There is also quite a difference in the dependence of lattice thermal conductivity on temperature between TiNiSn and $TiNi_{0.92}Sn$ before the onset of bipolar conduction at high temperature. It is known that the flatter the temperature dependence of the lattice thermal conductivity, the stronger the phonon scattering by point defects.[38] Therefore, Ni interstitials are responsible for the much lower lattice thermal conductivity of TiNiSn. To conclude, the striking differences in the bandgap and the electrical and thermal properties between TiNiSn and $TiNi_{0.92}Sn$ demonstrate the successful manipulation of the Ni interstitials, which provides a platform for us to further optimize the performance of the TiNiSn-based thermoelectric materials.

To investigate the effect of manipulation of the Ni interstitials on the electrical properties, external doping was introduced

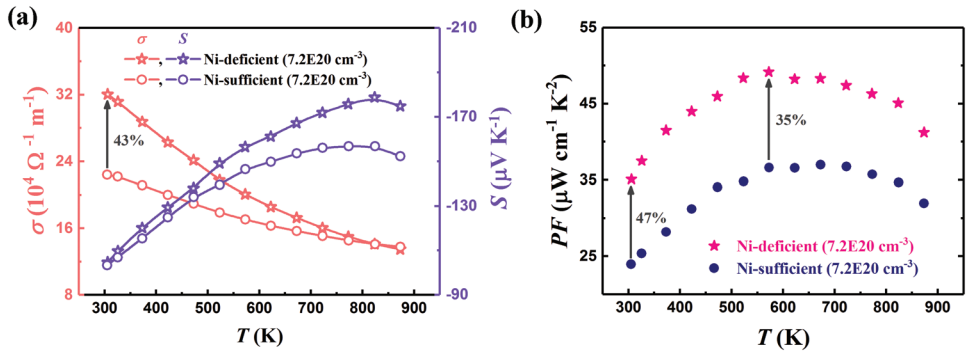


**Figure 3.** Comparison of electrical properties between Ta-doped Ni-deficient and Ni-sufficient compositions with similar Hall carrier concentration ≈$7.2 \times 10^{20}$ cm$^{-3}$ at room temperature. Temperature-dependent a) electrical conductivity and Seebeck coefficient and b) power factor.

in $TiNi_{0.92}Sn$ and TiNiSn, labeled Ni-deficient and Ni-sufficient compositions, respectively. Tantalum was employed as the impurity dopant and the carrier concentration was fixed at ≈$7.2 \times 10^{20}$ cm$^{-3}$ for better comparison. The $\sigma$ of the Ni-deficient composition is noticeably higher than that of the Ni-sufficient composition until the temperature reaches 800 K, as shown in **Figure 3**a. While it shows 43% improvement at room temperature, it almost converges with that of the Ni-sufficient composition when the temperature is above 800 K, which can be mainly ascribed to the higher carrier concentration in the Ni-sufficient composition. It is known that interstitial Ni atoms are capable of supplying more electrons as the temperature increases.[22] It should be noted that the $|S|$ of the Ni-sufficient composition is lower than that of the Ni-deficient composition at high temperature, which is also caused by the increased carrier concentration in the Ni-sufficient composition. Although the $\sigma$ values of both the compositions converge above 800 K, the larger $|S|$ of the Ni-deficient composition still favors a higher power factor at high temperatures. Impressively, the optimized electrical properties enable the significantly enhanced power factor (PF) of the Ni-deficient composition over the whole temperature range, where the room-temperature and peak *PF* values show 47% and 35% improvement over those of the Ni-sufficient composition, respectively, as shown in Figure 3b. These positive results highlight the beneficial contribution of Ni interstitial manipulation in improving the electrical properties and encourage us to uncover the thermoelectric performance of Ta-doped $TiNi_{0.92}Sn$. According to XRD spectra, all samples of $Ti_{1-\gamma}Ta_\gamma Ni_{0.92}Sn$ ($\gamma$ = 0.01, 0.02, 0.025, 0.03, and 0.05) possess the pure half-Heusler phase, as shown in Figure S3 (Supporting Information). The temperature dependence of $S$ and $\sigma$ are plotted in **Figure 4**a,b, respectively. With increasing $\gamma$, the $|S|$ decreases and the $\sigma$ increases, indicating that refractory Ta can act as an effective electron donor. For $TiNi_{0.92}Sn$, the $\sigma$–$T$ curve shows an intrinsic semiconductor behavior. For the samples with higher doping content, the $\sigma$ monotonically decreases at elevated temperatures, which is the typical behavior of any degenerate semiconductor. Figure 4c presents the temperature-dependent PF of $Ti_{1-\gamma}Ta_\gamma Ni_{0.92}Sn$, showing the peak value of ≈50 μW cm$^{-1}$ K$^{-2}$, which exceeds that of any other reported TiNiSn-based materials and is comparable with the best n-type half-Heusler compounds.

To determine the origin of the superior PF, the Hall mobility ($\mu_H$) of $Ti_{1-\gamma}Ta_\gamma Ni_{0.92}Sn$ (labeled Ni-deficient samples) is plotted versus carrier concentration ($n_H$) in Figure 4d, including the data of Ni-sufficient samples, i.e., $Ti_{1-\gamma}Ta_\gamma NiSn$ (this work, temperature-dependent thermoelectric properties are shown in Figure S4 in the Supporting Information), $TiNi_{1+z}Sn$,[15] $TiNi_{1.06}Sn_{1-z}Sb_z$,[16] $TiNiCu_zSn$,[17] and $(TiNiSn)_{1-z}$ + $(MnNiSb)_z$.[14] It is worth noting that the $\mu_H$ of the Ni-deficient samples shows an increase of 34–251% in comparison to the Ni-sufficient samples. Such substantial enhancement of $\mu_H$ is mainly derived from the weakened atomic-disorder scattering by Ni interstitial manipulation. As clearly shown in Figure 4e, lower $\mu_H$ causes the inferior PF of the Ni-sufficient samples. In sharp contrast, the superior PF of the Ni-deficient samples relies on its significantly enhanced $\mu_H$. Additionally, strategies for PF improvement by engineering intrinsic defects have been applied to various thermoelectric materials,[39,40] especially p-type NbFeSb with an ultrahigh PF.[10] Consequently, benefiting from the successful manipulation of the Ni interstitials, decent average PF ($PF_{avg}$) has been achieved in Ni-deficient samples, showing 38–95% improvement compared with that of Ni-sufficient samples (Figure 4f).[14–17]

The temperature-dependent $\kappa$ and $\kappa_L + \kappa_{bp}$ values are shown in **Figure 5**a,b, respectively. With increasing $\gamma$, the reduction of $\kappa_L + \kappa_{bp}$ is visible, whereas $\kappa$ shows little difference with increasing $\gamma$ due to the greater contribution of electrons at a higher doping content. It should be noted that the temperature dependence of $\kappa_L + \kappa_{bp}$ in Ta-doped samples is flatter than that of the undoped sample, suggesting that an additional phonon scattering center is introduced. Based on the quantitative disorder scattering parameter presented in the inset of Figure 5b, strong mass fluctuation and strain field fluctuation between the Ti and Ta atoms are responsible for the dramatically reduced lattice thermal conductivity. As a result of the carrier mobility enhancement by Ni interstitial manipulation and the lattice thermal conductivity suppression by Ta external doping, a peak *ZT* of ≈0.73 is achieved in Ni-deficient samples (Figure 5c). In comparison to previously reported TiNiSn-based materials, our well-designed sample exhibits the best *ZT*, as shown in Figure 5d.[14–17]

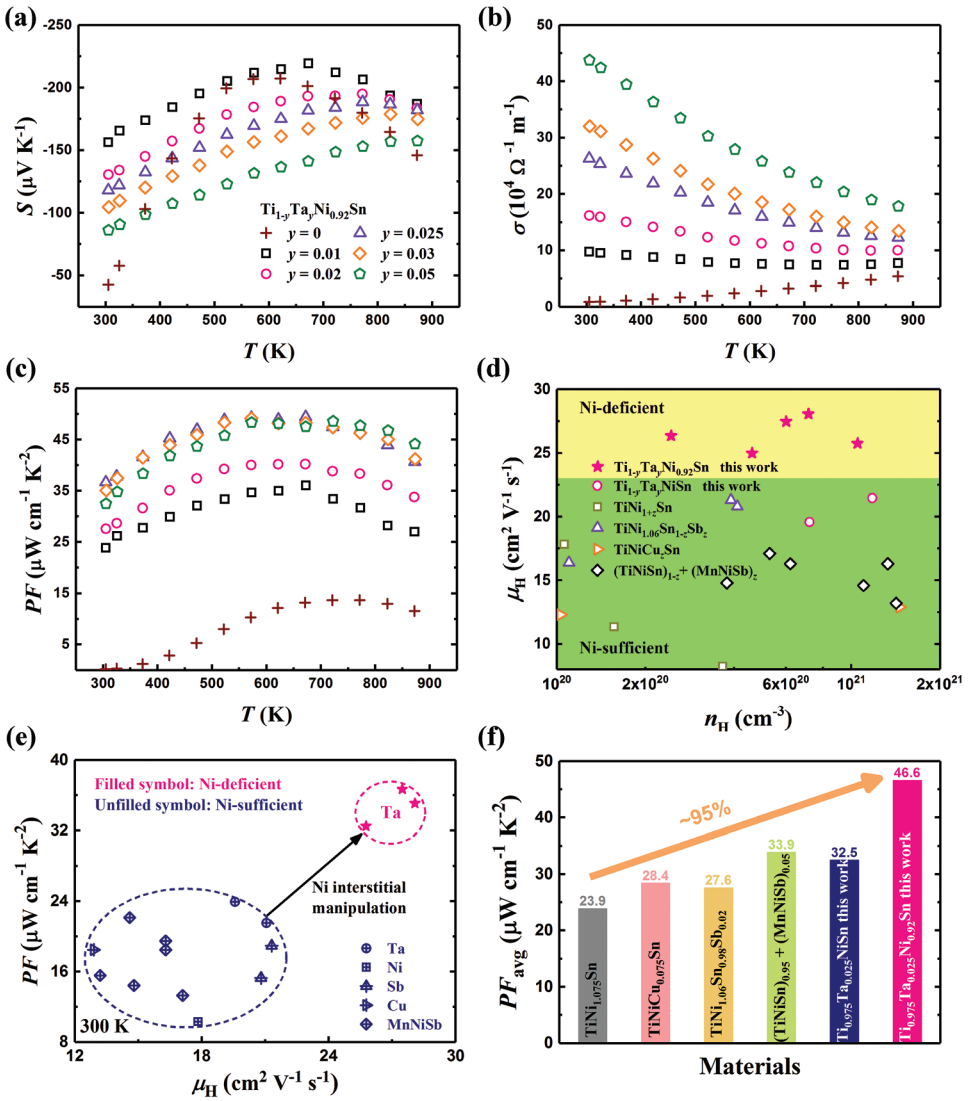


**Figure 4.** Temperature dependence of a) the Seebeck coefficient, b) electrical conductivity, and c) power factor of $Ti_{1-y}Ta_yNi_{0.92}Sn$ ($y$ = 0, 0.01, 0.02, 0.025, 0.03, and 0.05). d) Hall carrier concentration versus Hall mobility and e) Hall mobility versus power factor for Ni-deficient and Ni-sufficient samples. f) Comparison of average power factor values (over the range of 300–773 K) between Ni-deficient and Ni-sufficient samples. Data of $TiNi_{1+z}Sn$, $TiNi_{1.06}Sn_{1-z}Sb_z$, $TiNiCu_2Sn$, and $(TiNiSn)_{1-z}$ + (MnNiSb) are from refs. [14–17].

## 3. Conclusion

In summary, manipulation of Ni interstitials for minimizing the atomic disorder in TiNiSn-based materials is successfully demonstrated based on evidence from the varying structural, electrical, and thermal properties. In comparison to the Ni-sufficient TiNiSn-based materials, a substantial enhancement of carrier mobility is observed in Ni-deficient compositions, contributing to higher power factor with a peak value of ≈50 μW cm$^{-1}$ K$^{-2}$, comparable with the best reported n-type half-Heusler compounds. Moreover, our well-designed composition, employing both Ni interstitial manipulation and external Ta doping, shows a peak $ZT$ of ≈0.73, exceeding all other reported TiNiSn-based thermoelectric materials. We anticipate that the achievement of interstitial manipulation will spur further study on ingenious design at the atomic level for high-performance thermoelectric materials.

## 4. Experimental Section

*Synthesis*: Titanium sponge (Ti, 99.9%), nickel pellet (Ni, 99.999%), tin shot (Sn, 99.8%), and tantalum turning (Ta, 99.95%) were weighed according to the nominal compositions $TiNi_{1-x}Sn$ ($x$ = 0, 0.02, 0.04, 0.06, and 0.08) and $Ti_{1-y}Ta_yNi_{1-x}Sn$ ($x$ = 0, $y$ = 0.025, and 0.05; $x$ = 0.08, $y$ = 0.01, 0.02, 0.025, 0.03, and 0.05). The stoichiometrically weighed raw materials were melted in an arc furnace under argon protection. Remelting several times was necessary to form homogeneous ingots. High energy ball milling (SPEX 8000M Mixer/Mill) was then employed for 4 h to pulverize the ingots into fine powders. The obtained powders were loaded into a graphite die with an inner diameter of 12.7 mm and finally consolidated into disks by being held at 1273 K for 2 min via a hot-pressing process.

*Measurements—Thermoelectric Properties*: Simultaneous measurement for Seebeck coefficient ($S$) and electrical conductivity ($\sigma$) was conducted in a ZEM-3 system (ULVAC). Thermal conductivity was calculated according to $\kappa = D\rho C_p$. Thermal diffusivity ($D$) was measured in a laser

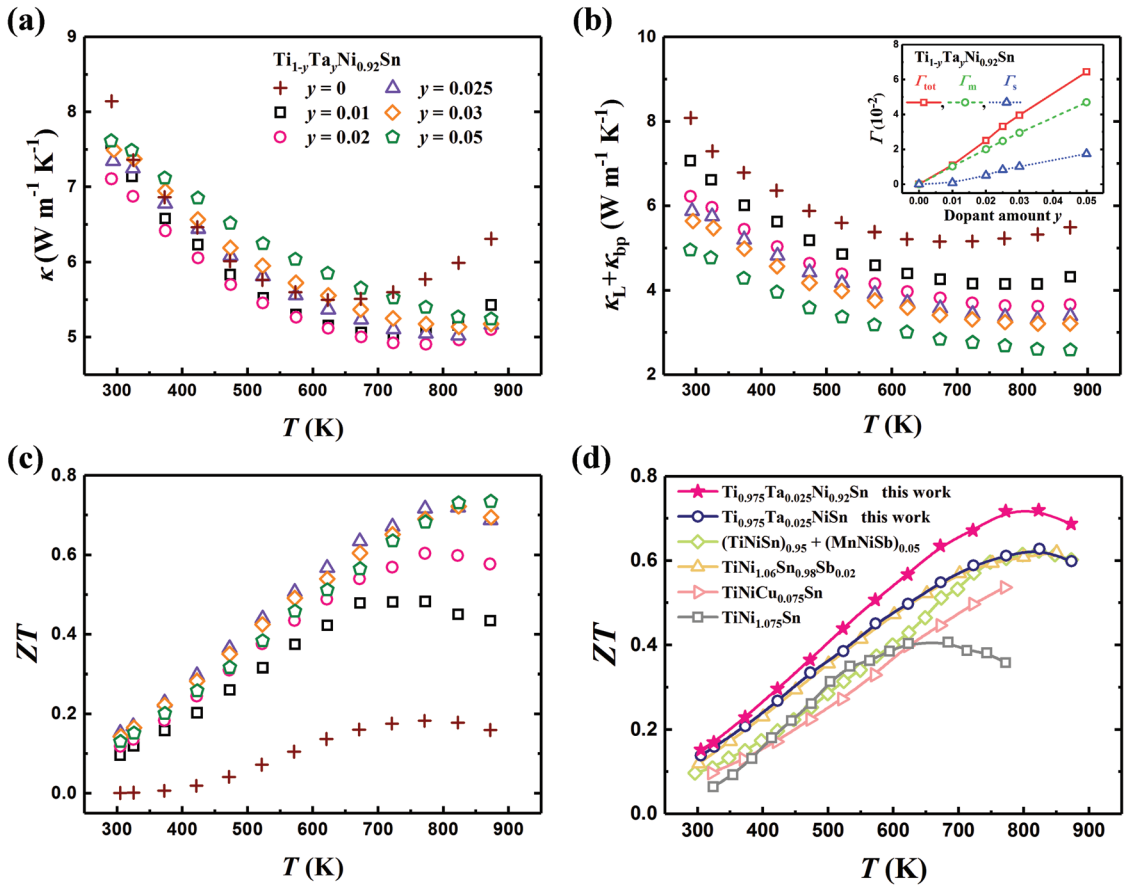


**Figure 5.** Temperature dependence of a) thermal conductivity, b) sum of lattice and bipolar thermal conductivity, and c) figure of merit (*ZT*) for $Ti_{1-y}Ta_yNi_{0.92}Sn$. d) Comparison of temperature-dependent *ZT* between Ni-deficient and Ni-sufficient samples.[14–17] The inset of (b) shows the disorder scattering parameter, $\Gamma_{tot} = \Gamma_M + \Gamma_S$, where $\Gamma_M$ (green circles) and $\Gamma_S$ (blue triangles) represent the disorder parameters from mass and strain field fluctuation, respectively.

flash instrument (LFA457, Netzsch). Mass density ($\rho$) was obtained by the Archimedes method. Specific heat capacity ($C_p$) was given by the Dulong–Petit law $C_p = 3k_B$ per atom. Hall carrier concentration ($n_H$) at room temperature was achieved by using the van der Pauw method in a physical properties measurement system (Quantum Design) with an electrical current of 8 mA and a magnetic field of ±3 T. Hall mobility ($\mu_H$) was determined by $\sigma = n_H e \mu_H$, where $e$ is the electronic charge.

*Measurements—Optical Measurement*: Fourier transform infrared spectroscopy (FTIR) was applied to reveal the optical bandgap according to the Kramers–Kronig analysis for the reflectance. The FTIR was performed by a Nicolet iS50 FT-IR spectrometer with a Spectra-Tech model 500 series variable angle specular reflectance accessory in the range of 400–7000 $cm^{-1}$.

*Measurements—Structure Characterizations*: XRD (PANalytical X'Pert Pro diffractometer with a Cu K$\alpha$ radiation source) was used to reveal the phases of the samples. The lattice parameters were deduced from Rietveld refinement. Scanning electron microscopy (JEOL 6340F) together with EDS were used to characterize the microstructure and elemental mapping.

## Supporting Information

Supporting Information is available from the Wiley Online Library or from the author.

## Acknowledgements

This work was supported by the U.S. Department of Energy under Grant Number DE-SC0010831; and was also supported by the National Natural Science Foundation of China (Grant No. 51272038) and the National Program on Key Basic Research Project (973 program) (Grant No. 2013CB933301). W.Y.R. acknowledges financial support from the Academic Exchange Special Fund at the University of Electronic Science and Technology of China.

## Conflict of Interest

The authors declare no conflict of interest.

## Keywords

average power factor, half-Heusler materials, interstitial manipulation, charge-carrier mobility, thermoelectrics

Received: February 13, 2019
Revised: April 9, 2019
Published online:

[1] a) J. Yang, H. M. Li, T. Wu, W. Q. Zhang, L. D. Chen, J. H. Yang, *Adv. Funct. Mater.* **2008**, *18*, 2880; b) H. Lin, L. A. Wray, Y. Xia, S. Xu, S. Jia, R. J. Cava, A. Bansil, M. Z. Hasan, *Nat. Mater.* **2010**, *9*, 546; c) T. J. Zhu, C. G. Fu, H. H. Xie, Y. T. Liu, X. B. Zhao, *Adv. Energy Mater.* **2015**, *5*, 1500588.

[2] a) G. Rogl, A. Grytsiv, M. Gürth, A. Tavassoli, C. Ebner, A. Wünschek, S. Puchegger, V. Soprunyuk, W. Schranz, E. Bauer, H. Müller, M. Zehetbauer, P. Rogl, *Acta Mater.* **2016**, *107*, 178; b) W. G. Zeier, J. Schmitt, G. Hautier, U. Aydemir, Z. M. Gibbs, C. Felser, G. J. Snyder, *Nat. Rev. Mater.* **2016**, *1*, 16032; c) S. Anand, K. Xia, V. I. Hegde, U. Aydemir, V. Kocevski, T. Zhu, C. Wolverton, G. J. Snyder, *Energy Environ. Sci.* **2018**, *11*, 1480; d) J. Mao, Z. H. Liu, J. W. Zhou, H. T. Zhu, Q. Zhang, G. Chen, Z. F. Ren, *Adv. Phys.* **2018**, *67*, 69.

[3] J. W. Zhou, H. T. Zhu, T. H. Liu, Q. C. Song, R. He, J. Mao, Z. H. Liu, W. Y. Ren, B. L. Liao, D. J. Singh, Z. F. Ren, G. Chen, *Nat. Commun.* **2018**, *9*, 1721.

[4] a) G. Joshi, R. He, M. Engber, G. Samsonidze, T. Pantha, E. Dahal, K. Dahal, J. Yang, Y. C. Lan, B. Kozinsky, Z. F. Ren, *Energy Environ. Sci.* **2014**, *7*, 4070; b) C. G. Fu, H. J. Wu, Y. T. Liu, J. Q. He, X. B. Zhao, T. J. Zhu, *Adv. Sci.* **2016**, *3*, 1600035; c) K. Xia, Y. Liu, S. Anand, G. J. Snyder, J. Xin, J. Yu, X. Zhao, T. Zhu, *Adv. Funct. Mater.* **2018**, *28*, 1705845.

[5] a) C. G. Fu, T. J. Zhu, Y. Z. Pei, H. H. Xie, H. Wang, G. J. Snyder, Y. Liu, Y. T. Liu, X. B. Zhao, *Adv. Energy Mater.* **2014**, *4*, 1400600; b) C. Hu, K. Xia, X. Chen, X. Zhao, T. Zhu, *Mater. Today Phys.* **2018**, *7*, 69; c) J. J. Yu, C. G. Fu, Y. T. Liu, K. Y. Xia, U. Aydemir, T. C. Chasapis, G. J. Snyder, X. B. Zhao, T. J. Zhu, *Adv. Energy Mater.* **2018**, *8*, 1701313.

[6] a) C. G. Fu, T. J. Zhu, Y. T. Liu, H. H. Xie, X. B. Zhao, *Energy Environ. Sci.* **2015**, *8*, 216; b) Y. Liu, C. Fu, K. Xia, J. Yu, X. Zhao, H. Pan, C. Felser, T. Zhu, *Adv. Mater.* **2018**, *30*, 1800881; c) C. Fu, Y. Liu, X. Zhao, T. Zhu, *Adv. Electron. Mater.* **2016**, *2*, 1600394; d) Q. Qiu, Y. Liu, K. Xia, T. Fang, J. Yu, X. Zhao, T. Zhu, *Adv. Energy Mater.* **2019**, *9*, 1803447.

[7] C. G. Fu, S. Q. Bai, Y. T. Liu, Y. S. Tang, L. D. Chen, X. B. Zhao, T. J. Zhu, *Nat. Commun.* **2015**, *6*, 8144.

[8] R. He, H. T. Zhu, J. Y. Sun, J. Mao, H. Reith, S. Chen, G. Schierning, K. Nielsch, Z. F. Ren, *Mater. Today Phys.* **2017**, *1*, 24.

[9] H. T. Zhu, R. He, J. Mao, Q. Zhu, C. H. Li, J. F. Sun, W. Y. Ren, Y. M. Wang, Z. H. Liu, Z. J. Tang, A. Sotnikov, Z. M. Wang, D. Broido, D. J. Singh, G. Chen, K. Nielsch, Z. F. Ren, *Nat. Commun.* **2018**, *9*, 2497.

[10] a) R. He, D. Kraemer, J. Mao, L. P. Zeng, Q. Jie, Y. C. Lan, C. H. Li, J. Shuai, H. S. Kim, Y. Liu, D. Broido, C. W. Chu, G. Chen, Z. F. Ren, *Proc. Natl. Acad. Sci. USA* **2016**, *113*, 13576; b) W. Y. Ren, H. T. Zhu, Q. Zhu, U. Saparamadu, R. He, Z. H. Liu, J. Mao, C. Wang, K. Nielsch, Z. M. Wang, Z. F. Ren, *Adv. Sci.* **2018**, *5*, 1800278.

[11] a) S. Öğüt, K. M. Rabe, *Phys. Rev. B* **1995**, *51*, 10443; b) S. Bhattacharya, A. L. Pope, R. T. Littleton, T. M. Tritt, V. Ponnambalam, Y. Xia, S. J. Poon, *Appl. Phys. Lett.* **2000**, *77*, 2476; c) P. Larson, S. D. Mahanti, M. G. Kanatzidis, *Phys. Rev. B* **2000**, *62*, 12754.

[12] a) R. A. Downie, D. A. MacLaren, R. I. Smith, J. W. Bos, *Chem. Commun.* **2013**, *49*, 4184; b) A. Page, C. Uher, P. F. Poudeu, A. Van der Ven, *Phys. Rev. B* **2015**, *92*, 174102; c) M. Gürth, A. Grytsiv, J. Vrestal, V. V. Romaka, G. Giester, E. Bauer, P. Rogl, *RSC Adv.* **2015**, *5*, 92270.

[13] a) M. Wambach, R. Stern, S. Bhattacharya, P. Ziolkowski, E. Müller, G. K. H. Madsen, A. Ludwig, *Adv. Electron. Mater.* **2016**, *2*, 1500208; b) G. Li, Q. An, U. Aydemir, W. A. Goddard Iii, M. Wood, P. Zhai, Q. Zhang, G. J. Snyder, *J. Mater. Chem. A* **2016**, *4*, 14625.

[14] T. Berry, C. Fu, G. Auffermann, G. H. Fecher, W. Schnelle, F. Serrano-Sanchez, Y. Yue, H. Liang, C. Felser, *Chem. Mater.* **2017**, *29*, 7042.

[15] S. A. Barczak, J. Buckman, R. I. Smith, A. R. Baker, E. Don, I. Forbes, J. G. Bos, *Materials* **2018**, *11*, 536.

[16] Y. Tang, X. Li, L. H. J. Martin, E. Cuervo Reyes, T. Ivas, C. Leinenbach, S. Anand, M. Peters, G. J. Snyder, C. Battaglia, *Energy Environ. Sci.* **2018**, *11*, 311.

[17] S. A. Barczak, J. E. Halpin, J. Buckman, R. Decourt, M. Pollet, R. I. Smith, D. A. MacLaren, J. G. Bos, *ACS Appl. Mater. Interfaces* **2018**, *10*, 4786.

[18] a) S.-W. Kim, Y. Kimura, Y. Mishima, *Intermetallics* **2007**, *15*, 349; b) T. Berry, S. Ouardi, G. H. Fecher, B. Balke, G. Kreiner, G. Auffermann, W. Schnelle, C. Felser, *Phys. Chem. Chem. Phys.* **2017**, *19*, 1543.

[19] H. Hazama, M. Matsubara, R. Asahi, T. Takeuchi, *J. Appl. Phys.* **2011**, *110*, 063710.

[20] R. A. Downie, R. I. Smith, D. A. MacLaren, J.-W. G. Bos, *Chem. Mater.* **2015**, *27*, 2449.

[21] a) H. H. Xie, H. Wang, Y. Z. Pei, C. G. Fu, X. H. Liu, G. J. Snyder, X. B. Zhao, T. J. Zhu, *Adv. Funct. Mater.* **2013**, *23*, 5123; b) S. Chen, K. C. Lukas, W. S. Liu, C. P. Opeil, G. Chen, Z. F. Ren, *Adv. Energy Mater.* **2013**, *3*, 1210.

[22] H. H. Xie, H. Wang, C. G. Fu, Y. T. Liu, G. J. Snyder, X. B. Zhao, T. J. Zhu, *Sci. Rep.* **2015**, *4*, 6888.

[23] a) Y. T. Liu, H. H. Xie, C. G. Fu, G. J. Snyder, X. B. Zhao, T. J. Zhu, *J. Mater. Chem. A* **2015**, *3*, 22716; b) G. Rogl, P. Sauerschnig, Z. Rykavets, V. V. Romaka, P. Heinrich, B. Hinterleitner, A. Grytsiv, E. Bauer, P. Rogl, *Acta Mater.* **2017**, *131*, 336; c) J. Mao, J. W. Zhou, H. T. Zhu, Z. H. Liu, H. Zhang, R. He, G. Chen, Z. F. Ren, *Chem. Mater.* **2017**, *29*, 867.

[24] T. Graf, C. Felser, S. S. P. Parkin, *Prog. Solid State Chem.* **2011**, *39*, 1.

[25] A. Berche, P. Jund, *Materials* **2018**, *11*, 868.

[26] a) Y. Z. Pei, A. F. May, G. J. Snyder, *Adv. Energy Mater.* **2011**, *1*, 291; b) L. You, Y. Liu, X. Li, P. Nan, B. Ge, Y. Jiang, P. Luo, S. Pan, Y. Pei, W. Zhang, G. J. Snyder, J. Yang, J. Zhang, J. Luo, *Energy Environ. Sci.* **2018**, *11*, 1848.

[27] a) Y. Pei, L. Zheng, W. Li, S. Lin, Z. Chen, Y. Wang, X. Xu, H. Yu, Y. Chen, B. Ge, *Adv. Electron. Mater.* **2016**, *2*, 1600019; b) L. Zheng, W. Li, S. Lin, J. Li, Z. Chen, Y. Pei, *ACS Energy Lett.* **2017**, *2*, 563; c) W. Li, L. L. Zheng, B. H. Ge, S. Q. Lin, X. Y. Zhang, Z. W. Chen, Y. J. Chang, Y. Z. Pei, *Adv. Mater.* **2017**, *29*, 1605887; d) F. Guo, B. Cui, Y. Liu, X. Meng, J. Cao, Y. Zhang, R. He, W. Liu, H. Wu, S. J. Pennycook, W. Cai, J. Sui, *Small* **2018**, *14*, 1802615; e) J. Tang, B. Gao, S. Lin, J. Li, Z. Chen, F. Xiong, W. Li, Y. Chen, Y. Pei, *Adv. Funct. Mater.* **2018**, *28*, 1803586.

[28] K. S. Kim, Y. M. Kim, H. Mun, J. Kim, J. Park, A. Y. Borisevich, K. H. Lee, S. W. Kim, *Adv. Mater.* **2017**, *29*, 1702091.

[29] a) W. Zhao, Z. Liu, Z. Sun, Q. Zhang, P. Wei, X. Mu, H. Zhou, C. Li, S. Ma, D. He, P. Ji, W. Zhu, X. Nie, X. Su, X. Tang, B. Shen, X. Dong, J. Yang, Y. Liu, J. Shi, *Nature* **2017**, *549*, 247; b) X. F. Meng, Z. H. Liu, B. Cui, D. D. Qin, H. Y. Geng, W. Cai, L. W. Fu, J. Q. He, Z. F. Ren, J. H. Sui, *Adv. Energy Mater.* **2017**, *7*, 1602582.

[30] a) G. J. Snyder, M. Christensen, E. Nishibori, T. Caillat, B. B. Iversen, *Nat. Mater.* **2004**, *3*, 458; b) L. T. Hung, D.-T. Ngo, L. Han, B. B. Iversen, H. Yin, N. Pryds, N. Van Nong, *Adv. Electron. Mater.* **2017**, *3*, 1700223.

[31] X. Shi, J. Yang, J. R. Salvador, M. Chi, J. Y. Cho, H. Wang, S. Bai, J. Yang, W. Zhang, L. Chen, *J. Am. Chem. Soc.* **2011**, *133*, 7837.

[32] Y. G. Yu, X. Zhang, A. Zunger, *Phys. Rev. B* **2017**, *95*, 085201.

[33] Z. H. Liu, J. Mao, S. Y. Peng, B. Q. Zhou, W. H. Gao, J. H. Sui, Y. Z. Pei, Z. F. Ren, *Mater. Today Phys.* **2017**, *2*, 54.

[34] F. G. Aliev, N. B. Brandt, V. V. Moshchalkov, V. V. Kozyrkov, R. V. Skolozdra, A. I. Belogorokhov, *Z. Phys. B: Condens. Matter* **1989**, *75*, 167.

[35] J. Schmitt, Z. M. Gibbs, G. J. Snyder, C. Felser, *Mater. Horiz.* **2015**, *2*, 68.

[36] R. A. Downie, S. A. Barczak, R. I. Smith, J. W. G. Bos, *J. Mater. Chem. C* **2015**, *3*, 10534.

 

[37] K. Miyamoto, A. Kimura, K. Sakamoto, M. Ye, Y. Cui, K. Shimada, H. Namatame, M. Taniguchi, S.-i. Fujimori, Y. Saitoh, E. Ikenaga, K. Kobayashi, J. Tadano, T. Kanomata, *Appl. Phys. Express* **2008**, *1*, 081901.

[38] H. Takaki, K. Kobayashi, M. Shimono, N. Kobayashi, K. Hirose, N. Tsujii, T. Mori, *Mater. Today Phys.* **2017**, *3*, 85.

[39] a) X. Liu, L. Xi, W. Qiu, J. Yang, T. Zhu, X. Zhao, W. Zhang, *Adv. Electron. Mater.* **2016**, *2*, 1500284; b) J. Mao, Y. X. Wu, S. W. Song, Q. Zhu, J. Shuai, Z. H. Liu, Y. Z. Pei, Z. F. Ren, *ACS Energy Lett.* **2017**, *2*, 2245; c) J. Shuai, J. Mao, S. W. Song, Q. Zhu, J. F. Sun, Y. M. Wang, R. He, J. W. Zhou, G. Chen, D. J. Singh, Z. F. Ren, *Energy Environ. Sci.* **2017**, *10*, 799.

[40] a) J. Mao, J. Shuai, S. W. Song, Y. X. Wu, R. Dally, J. W. Zhou, Z. H. Liu, J. F. Sun, Q. Y. Zhang, C. Dela Cruz, S. Wilson, Y. Z. Pei, D. J. Singh, G. Chen, C. W. Chu, Z. F. Ren, *Proc. Natl. Acad. Sci. USA* **2017**, *114*, 10548; b) Q. Song, P. Qiu, H. Chen, K. Zhao, M. Guan, Y. Zhou, T. R. Wei, D. Ren, L. Xi, J. Yang, Z. Chen, X. Shi, L. Chen, *Mater. Today Phys.* **2018**, *7*, 45; c) X. Zhang, J. Li, X. Wang, Z. Chen, J. Mao, Y. Chen, Y. Pei, *J. Am. Chem. Soc.* **2018**, *140*, 15883.